International Journal of Pressure Vessels and Piping 87 (2010) 365–372

Contents lists available at ScienceDirect

International Journal of Pressure Vessels and Piping

journal homepage: www.elsevier.com/locate/ijpvp

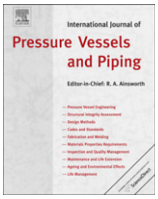

Cyclic thermo-mechanical material modelling and testing of 316 stainless steel

C.J. Hyde [a], [*], W. Sun [a], S.B. Leen [b]

[a] Department of Mechanical, Materials and Manufacturing Engineering, University of Nottingham, University Park, Nottingham NG7 2RD, UK
[b] Department of Mechanical and Biomedical Engineering, Nun's Island, National University of Ireland, Galway, Republic of Ireland

ARTICLE INFO

Article history:
Received 30 November 2008
Accepted 30 January 2010

Keywords:
Thermo-mechanical fatigue
Creep
Plasticity
Chaboche unified viscoplasticity model
316 Stainless steel

ABSTRACT

A programme of cyclic mechanical testing of a 316 stainless steel, at temperatures of up to 600 °C under isothermal conditions, for the identification of material constitutive constants, has been carried out using a thermo-mechanical fatigue test machine (with induction coil heating). The constitutive model adopted is a modified Chaboche unified viscoplasticity model, which can deal with both cyclic effects, such as combined isotropic and kinematic hardening, and rate-dependent effects, associated with viscoplasticity. The characterisation of 316 stainless steel is presented and compared with results from tests consisting of cyclic isothermal, as well as in-phase and out-of-phase thermo-mechanical fatigue conditions, using interpolation between the isothermal material constants to predict the material behaviour under anisothermal conditions.

1. Introduction

Thermo-mechanical fatigue, or TMF, has received an increasing amount of attention over the last thirty years. The two most common experimental TMF waveforms are in-phase (IP) and out-of-phase (OP) as shown in Fig. 1, where φ represents the phase angle between the strain and temperature waveforms. Some of the areas of particular interest have included the effect of phase angle on the life and failure of materials undergoing TMF as shown by Pahlavanyali et al. [1], TMF behaviour of superalloys, e.g. Evans et al. [2], TMF of specific components, e.g. Harrison et al. [3], and crack growth under TMF conditions, e.g. Dai et al. [4].

Unified material models are considered as a robust way of modelling the behaviour of materials where both rate-independent and rate-dependent effects occur simultaneously, e.g. for high-temperature cyclic loading. The Chaboche unified viscoplasticity model, for example, includes both non-linear isotropic hardening and kinematic hardening, for cyclic phenomena such as hardening and the Bauschinger effect [5], as well as creep effects. This model was first published by Chaboche and Rousselier in 1983 [6,7] and is discussed further by LeMaitre and Chaboche [8]. Since then the model has been widely used, for example, Tong and Zhan et al. [9–14].

The present paper is particularly concerned with the application of the Chaboche model to anisothermal conditions. In order to achieve this, isothermal tests have been performed to obtain the material constants at a range of temperatures. At each temperature, the model has been used to simulate isothermal cyclic conditions and the predictions compared to the experimental data. Each material constant was then represented as a function of temperature for simulation of the anisothermal IP and OP TMF conditions. The results from these simulations are compared with experimental TMF data. Examples of previous work on TMF of stainless steel include that of Santacreu et al. [15] concerned with automotive exhaust applications and Rau et al. [16] in the exploration of more complex testing conditions, to understand more realistic behaviours of materials in industrial use.

2. Experimental programme

All of the results presented have been obtained using 316 stainless steel specimens. Table 1 shows the chemical composition of the 316 stainless steel obtained as an average of three spark emission tests performed on material from the same batch as the specimens.

2.1. TMF machine and thermal calibration

The TMF machine used in this work is an Instron 8862 thermo-mechanical fatigue system which utilises radio-frequency (RF)

---

[*] Corresponding author
E-mail address: eaxch@nottingham.ac.uk (C.J. Hyde).

0308-0161/$ – see front matter © 2010 Elsevier Ltd. All rights reserved.
doi:10.1016/j.ijpvp.2010.03.007

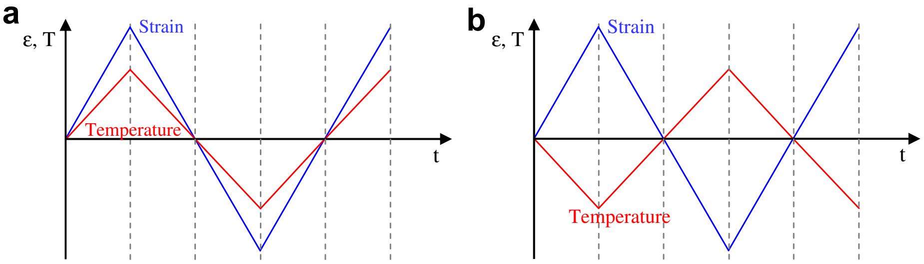

Fig. 1. Schematic representations of an: (a) in-phase TMF waveform, $\varphi = 0^\circ$ and (b) out-of-phase TMF waveform, $\varphi = 180^\circ$.

Table 1
Chemical compositions of the 316 stainless steel (wt%).

Fe	Cr	Ni	Mo	Mn	Si	Cu	V	Co	S	C	Nb	P	W	Ti	Al
66.4	16.8	11.8	2.15	1.42	0.5	0.49	0.08	0.07	0.03	0.02	0.02	0.01	<0.02	0.01	0.01

induction heating and forced air cooling through the centre of the specimen in order to achieve rapid heating and cooling, respectively. The maximum achievable load from the machine is 35 kN (limited by the grips) and the maximum allowable temperature is 1100 °C.

The requirement for temperature uniformity in the gauge section of the specimen during testing was that the entire gauge section was within ±10 °C of the target temperature. Therefore initial experimental work was concerned with achieving this.

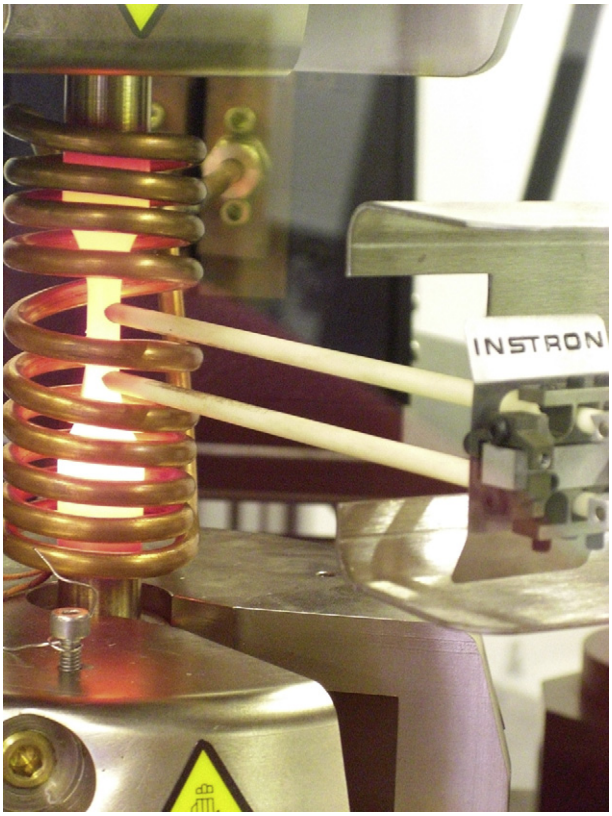

Fig. 2. Photograph of the heated specimen, induction coil and extensometer setup on the TMF machine.

Thermocouples were placed along the gauge section of the specimen in order to monitor the axial, as well as the circumferential temperature gradients within the specimen gauge section during a series of ramp and hold, as well as cyclic thermal testing. Initially the results were not within this tolerance, with axial deviations of up to ±30 °C from the target temperature. Therefore new coil designs were investigated.

A key problem faced was achieving the temperature uniformity required whilst leaving enough space between the turns of the coil for the attachment of the extensometer to the gauge section of the specimen. Fig. 2 shows the final coil design which gives temperature uniformity throughout the gauge section to within the tolerance required for target temperatures ranging from 200 °C to 1000 °C. Fig. 3 shows the temperature uniformity results obtained using this coil and a 316 stainless steel specimen for a target temperature of 800 °C.

2.2. Isothermal cyclic testing

Isothermal cyclic tests were carried out at temperatures of 300 °C, 500 °C, 550 °C and 600 °C. Fig. 4 shows the specimen geometry used in these tests. At each temperature, the test was performed for fifty loops at four strain ranges, i.e. stepped strain-range testing (200 loops in total), using one specimen for each temperature. Example results at 600 °C from these tests are shown in Fig. 5. It can be seen that the majority of the material hardening occurred at the first and lowest strain range (±0.3%). Therefore these test results at a strain range of ±0.3% were used to obtain the material constants for the Chaboche unified viscoplasticity model (see Sections 3 and 4) for each temperature.

2.3. TMF

The results of two TMF tests, carried out under IP and OP conditions are presented. The IP TMF test was carried out using a strain range, $\Delta\varepsilon$, of ±0.5% and a temperature range, ΔT, of 300 °C with a minimum temperature, $T_{\min}$, of 300 °C and a maximum temperature, $T_{\max}$, of 600 °C. A saw-tooth waveform was used as shown in Fig. 1a and the results for this test are shown in Fig. 6a. The OP TMF test was carried out using a strain range, $\Delta\varepsilon$, of ±0.6% and the same temperature wave as the IP TMF test, the saw-tooth waveform was is shown in Fig. 1b and the results for this test are shown in Fig. 6b.

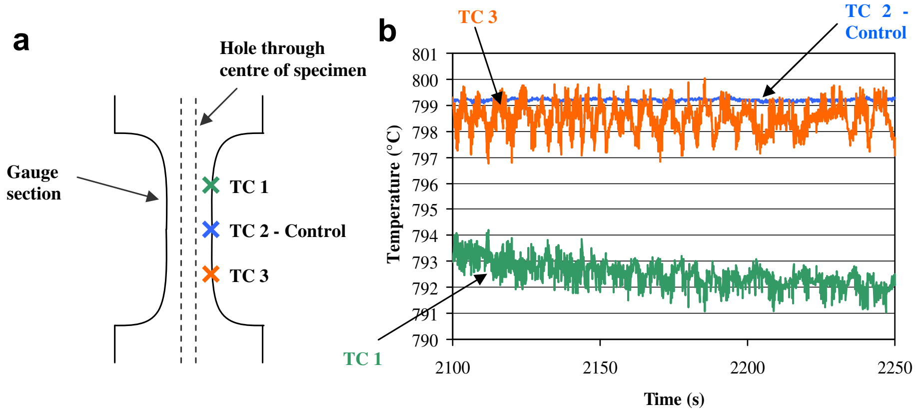

Fig. 3. Thermocouple positions and thermal uniformity results using the final coil.

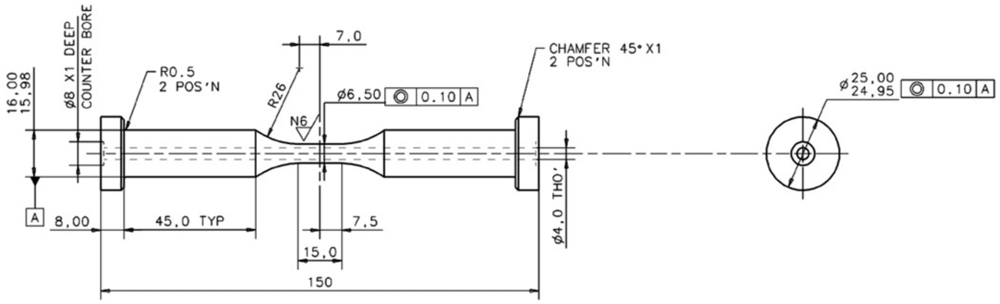

Fig. 4. Specimen geometry used on the TMF machine.

3. Definition of the material behaviour model

The Chaboche unified viscoplasticity model has been chosen to represent the uniaxial cyclic material behaviour of 316 stainless steel. The uniaxial form of the model is as follows:

$$\dot{\varepsilon}_{\mathrm{p}} = \left\langle \frac{f}{Z} \right\rangle^{n} \mathrm{sgn}(\sigma - \chi) \tag{1}$$

where, $\mathrm{sgn}(x) = \begin{cases} 1 & x > 0 \\ 0 & x = 0 \\ -1 & x < 0 \end{cases}$ and $\langle x \rangle = \begin{cases} x & x \geq 0 \\ 0 & x < 0 \end{cases}$

and

$$f = |\sigma - \chi| - R - k \tag{2}$$

where the elastic domain is defined by $f \leq 0$ and the inelastic domain by $f > 0$

$$\dot{\chi}_{\mathrm{i}} = C_{\mathrm{i}}(a_{\mathrm{i}}\dot{\varepsilon}_{\mathrm{p}} - \chi_{\mathrm{i}}\dot{p}) \tag{3}$$

where $i = 1, 2$

$$\chi = \chi_1 + \chi_2 \tag{4}$$

$$\dot{R} = b(Q - R)\dot{p} \tag{5}$$

$$\sigma_{\mathrm{v}} = Z\dot{p}^{1/n} \tag{6}$$

$$\dot{p} = |\dot{\varepsilon}_{\mathrm{p}}| \tag{7}$$

$$\sigma = \chi + (R + k + \sigma_{\mathrm{v}})\mathrm{sgn}(\sigma - \chi) = E(\varepsilon - \varepsilon_{\mathrm{p}}) \tag{8}$$

Equation (1), the viscoplastic flow rule, is the governing equation within the model. As can be seen from equations (2) to (8), all of the other model variables, such as those used for calculating both types of hardening (isotropic, R and kinematic, χ) and viscous stress, σ_{v}, are dependent on the value of plastic strain, ε_{p}, calculated from this viscoplastic flow rule. Equation (2) is the yield criterion for the model.

As previously mentioned, this model takes account of both kinematic hardening and isotropic hardening. Fig. 7 shows the physical meaning of both types of hardening and the effect they have on the yield surface, both types of hardening are shown in three-dimensional (principle) stress space. When the stress state within the material causes the edge of the yield surface to be reached, kinematic hardening, implemented by equations (3) and

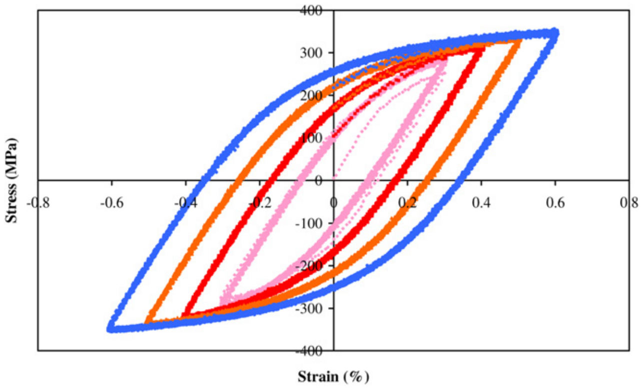

Fig. 5. Isothermal cyclic test results at 600 °C.

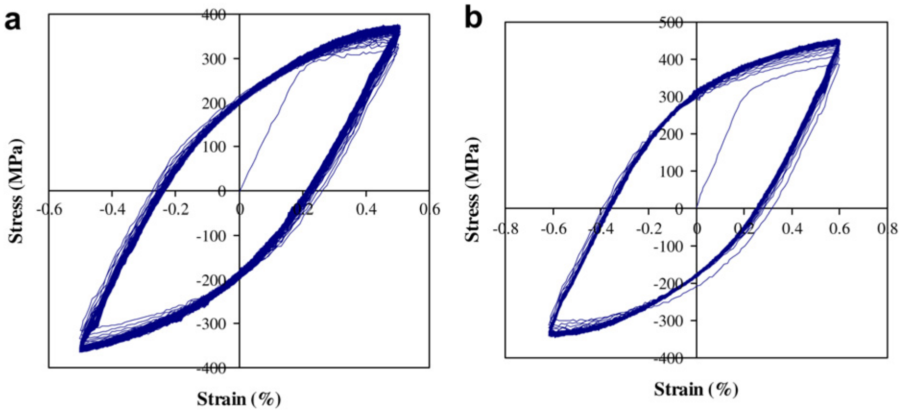

Fig. 6. Experimental TMF data: (a) in-phase and (b) out-of-phase.

(4), is represented as the movement of the yield surface, as shown in Fig. 7a. Isotropic hardening, implemented by equation (5), represents the growth of the yield surface, as shown in Fig. 7b.

Equation (6) defines the viscous stress, which takes the form of the widely used Norton creep law. Equation (7) shows that the variable, p, used in the calculation of many of the other variables is the accumulated plastic strain, ε_p.

The above model has been implemented in Matlab which is a top level programming language.

4. Identification of the material constants

In total, the material model requires the identification of 10 material constants. Within this section are brief descriptions of the methodologies used in calculating these constants, following the developments detailed in [11].

4.1. *Initial yield stress, k and Young's modulus, E*

From the initial experimental tensile curve, Young's modulus, E, is taken as the gradient of the initial linear region. The initial yield stress, k, can be estimated as the stress value at the point at which the data begins to deviate from this initial linear region.

4.2. *Isotropic hardening parameters, Q and b*

Equation (5) for the rate of isotropic hardening can be integrated with respect to time to give the following equation:

$$R = Q\left(1 - e^{-bp}\right) \tag{9}$$

Equation (9) shows that as the accumulated plastic strain, p, increases, R exponentially approaches saturation to a value of Q. Therefore, assuming that the material hardening is entirely due to isotropic hardening and plotting R against the accumulated plastic strain, the saturated value of R is identified as Q, as shown in Fig. 8. Then choosing a point roughly half way into the transient region of the hardening behaviour, shown circled in Fig. 8, the corresponding values of R and p are identified. These values (along with the calculated value of Q) are then put into the following equation, which is simply a rearranged version of equation (9) for b. By choosing this point roughly half way into the transient region of the hardening behaviour, the value of b calculated forces the model to go through this point and with the model saturating at the value of Q, the result is a close model fit to the experimental data as shown in Fig. 8.

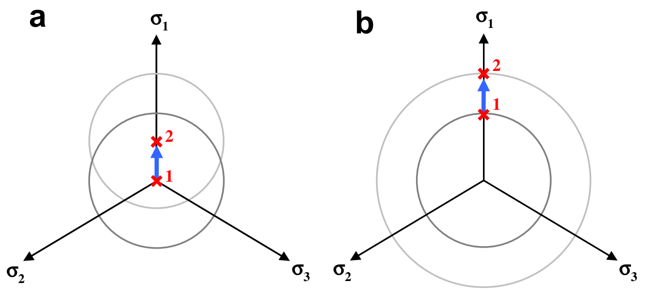

Fig. 7. Schematic representations of hardening behaviour: (a) kinematic and (b) isotropic.

$$b = \left[\frac{\ln(1 - R/Q)}{p}\right] \tag{10}$$

4.3. *Kinematic hardening parameters, a_1, C_1, a_2 and C_2*

Equation (3) for the rate of kinematic hardening can be integrated, with respect to time, to give the following equations:

$$\chi_1 = a_1\left(1 - e^{-C_1\varepsilon_p}\right) \tag{11}$$

$$\chi_2 = a_2\left(1 - e^{-C_2\varepsilon_p}\right) \tag{12}$$

Substituting equations (11) and (12) into equation (8) gives:

$$\sigma = a_1\left(1 - e^{-C_1\varepsilon_p}\right) + a_2\left(1 - e^{-C_2\varepsilon_p}\right) + R + k + \sigma_v \tag{13}$$

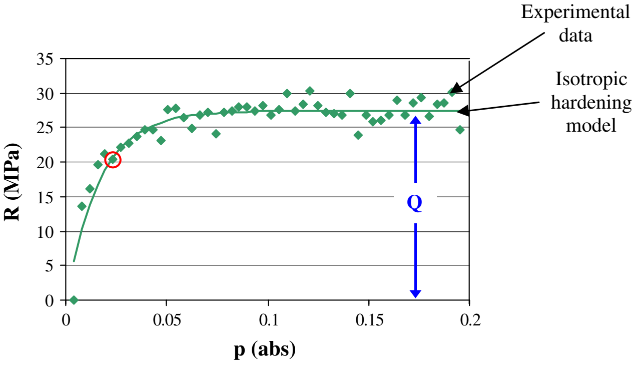

Fig. 8. Isotropic hardening variable R versus p for 316 stainless steel at 600 °C.

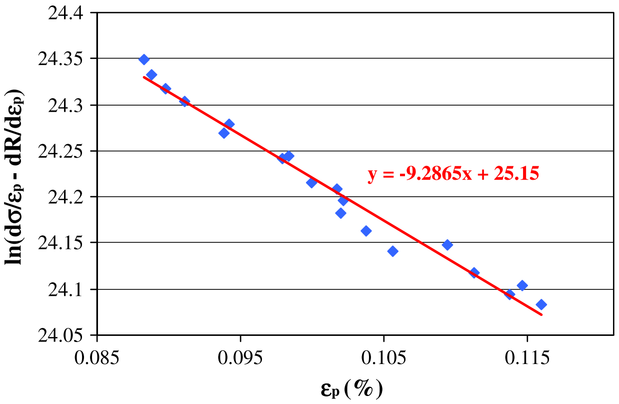

Fig. 9. Plot used in the calculation of the kinematic hardening material constants a_2 and C_2 for 316 stainless steel at 600 °C.

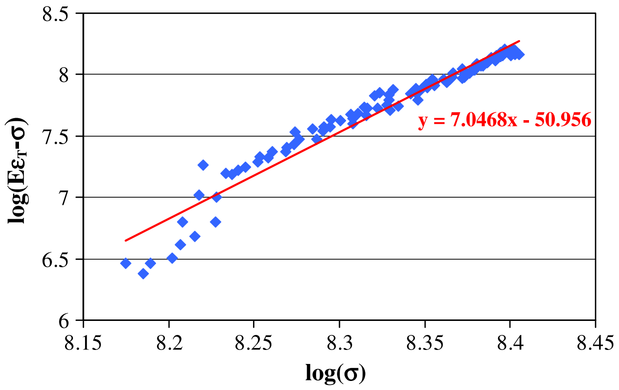

Fig. 10. Plot of log $(E\varepsilon_T - \sigma)$ vs. used in determining the constants used in the Ramberg–Osgood equation.

Table 2
Ramberg–Osgood constants for 316 stainless steel at multiple temperatures.

T (°C)	ε_0 (%)	σ_0 (MPa)	n_0
300	0.21803	337.61	7.2409
500	0.20277	295.11	6.1627
550	0.21779	307.65	7.2846
600	0.19212	267.26	7.0468

If the later stages of hardening are considered, it can be assumed that χ_1(and therefore a_1 and C_1) has a negligible effect on the hardening and therefore the kinematic hardening is dominated by χ_2 (a_2 and C_2). Therefore, equation (13) can be simplified to:

$$\sigma = a_2\left(1 - e^{-C_2\varepsilon_p}\right) + R + k + \sigma_v \tag{14}$$

Differentiating equation (14) with respect to ε_p, rearranging and taking natural logs of both sides gives the following equation (assuming yield stress, k, and viscous stress, σ_v, to be constants):

$$\ln\left(\frac{\partial\sigma}{\partial\varepsilon_p} - \frac{\partial R}{\partial\varepsilon_p}\right) = -C_2\varepsilon_p + \ln(a_2 C_2) \tag{15}$$

Therefore plotting $\ln(\partial\sigma/\partial\varepsilon_p - \partial R/\partial\varepsilon_p)$ vs. ε_p as shown in Fig. 9 allows the identification of C_2 from the gradient and a_2 from the y-axis intercept. Similarly, a_1 and C_1 can be found, for the lower strain region, from equation (13), having already identified a_2 and C_2 [11].

In order to perform this fit to the data, it is necessary to obtain expressions for $\partial\sigma/\partial\varepsilon_p$ and $\partial R/\partial\varepsilon_p$, as functions of ε_p, to use in equation (15). For the initial tensile curve (the first quarter cycle), $p = \varepsilon_p$, which can be substituted into equation (9). This expression can then be differentiated with respect to ε_p, to give the following:

$$\frac{\partial R}{\partial\varepsilon_p} = bQe^{-b\varepsilon_p} \tag{16}$$

The calculation of $\partial\sigma/\partial\varepsilon_p$ is more complicated. Taking $d\sigma/d\varepsilon_p$, multiplying by dt/dt and $d\varepsilon_T/d\varepsilon_T$, then rearranging gives the following:

$$\frac{d\sigma}{d\varepsilon_p} = \frac{d\sigma}{d\varepsilon_T}\cdot\frac{1}{\dot{\varepsilon}_p}\cdot\dot{\varepsilon}_T \tag{17}$$

Hence, expressions for $d\sigma/d\varepsilon_T$ and $\dot{\varepsilon}_p$ are required. The value of $\dot{\varepsilon}_T$ is controlled during testing as hence is known. To obtain $\dot{\varepsilon}_p$, Hooke's law, $\varepsilon_e = \sigma/E$, is substituted into the following equation for total strain:

$$\varepsilon_T = \varepsilon_e + \varepsilon_p \tag{18}$$

Rearranging equation (18) and differentiating it with respect to time gives the following:

$$\frac{d\varepsilon_p}{dt} = \frac{d\varepsilon_T}{dt} - \frac{d\sigma}{dt}\cdot\frac{1}{E} \tag{19}$$

Multiplying the final term in equation (19) by $d\varepsilon_T/d\varepsilon_T$ and rearranging gives the following:

$$\dot{\varepsilon}_p = \dot{\varepsilon}_T\left(1 - \frac{1}{E}\cdot\frac{d\sigma}{d\varepsilon_T}\right) \tag{20}$$

In order to obtain an expression for $d\sigma/d\varepsilon_T$, a smoothing function is needed to eliminate complications caused by scatter in the

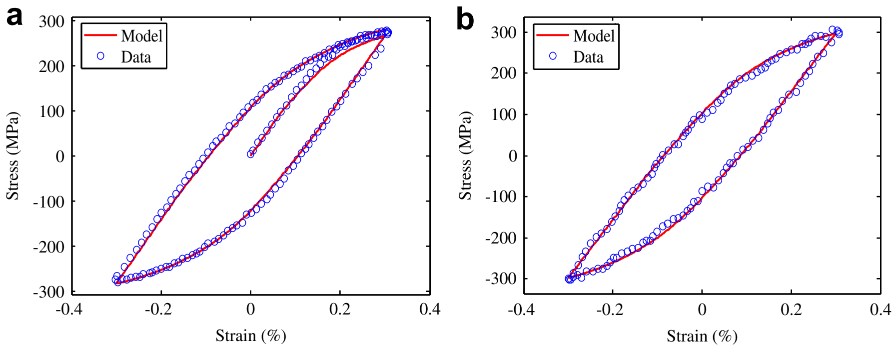

Fig. 11. Comparison of model predictions of cyclic $\sigma - \varepsilon$ behaviour to isothermal experimental data at 550 °C. (a) Monotonic tensile curve and 1st loop and (b) saturated loop.

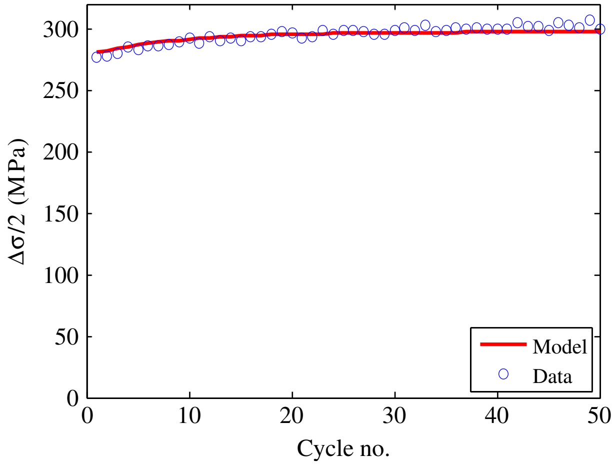

Fig. 12. Comparison of model predictions of hardening behaviour to isothermal experimental data at 550 °C.

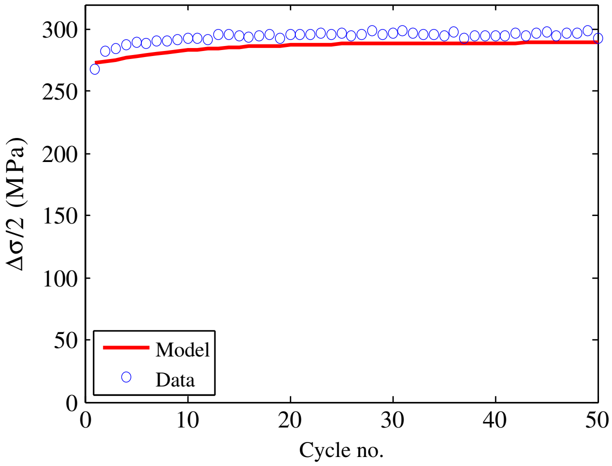

Fig. 14. Comparison of model predictions of hardening behaviour to isothermal experimental data at 600 °C.

experimental data, which could cause negative values of $d\sigma/d\varepsilon_T$ to be obtained at some strain values. The smoothing function used in this case is the Ramberg–Osgood equation, i.e.:

$$\frac{\varepsilon_T}{\varepsilon_0} = \frac{\sigma}{\sigma_0} + \left(\frac{\sigma}{\sigma_0}\right)^{n_0} \tag{21}$$

$$\varepsilon_0 = \frac{\sigma_0}{E} \tag{22}$$

Equation (22) can be substituted into equation (21) to give:

$$\frac{E\varepsilon_T}{\sigma_0} = \frac{\sigma}{\sigma_0} + \left(\frac{\sigma}{\sigma_0}\right)^{n_0} \tag{23}$$

which can then be differentiated with respect to ε_T to give:

$$\frac{d\sigma}{d\varepsilon_T} = \frac{\sigma_0}{\varepsilon_0\left(1 + n_0\left(\frac{\sigma}{\sigma_0}\right)^{n_0-1}\right)} \tag{24}$$

The Ramberg–Osgood constants, namely ε_0, σ_0 and n_0, can be found by rearranging and taking logs of both sides of equation (23) to give the following:

$$\log(E\varepsilon_T - \sigma) = n_0\log\sigma + (1 - n_0)\log\sigma_0 \tag{25}$$

Therefore, plotting $\log(E\varepsilon_T - \sigma)$ vs. $\log\sigma$ allows the identification of n (gradient) and σ_0 (from the y-axis intercept). An example of this plot for a temperature of 600 °C is shown by Fig. 10. Equation (22) can then be used to determine ε_0. Table 2 shows the Ramberg–Osgood constants calculated for the four temperatures.

4.4. Creep constants, Z and n

Typical values of Z and n have been taken from literature, such as Ryu [17] and Hyde [18–20]. The Matlab computer program for the model was run varying these constants around the typical values in order to obtain good fits to the model; this resulted in the constants presented in Table 2.

4.5. Material constants

Table 2 summarises the material constants identified from the isothermal test data for the four temperatures (Fig. 13).

5. Model predictions

5.1. Comparison of model predictions to isothermal experimental results

Figs. 11–14 show comparisons of the experimental and model results for the isothermal cases of 550 °C and 600 °C for a strain range of ±0.3%. The figures show the monotonic tensile curve and first cycle, saturated cycle and hardening behaviour of the material. Fig. 15 shows the complete predicted history (fifty loops) from the

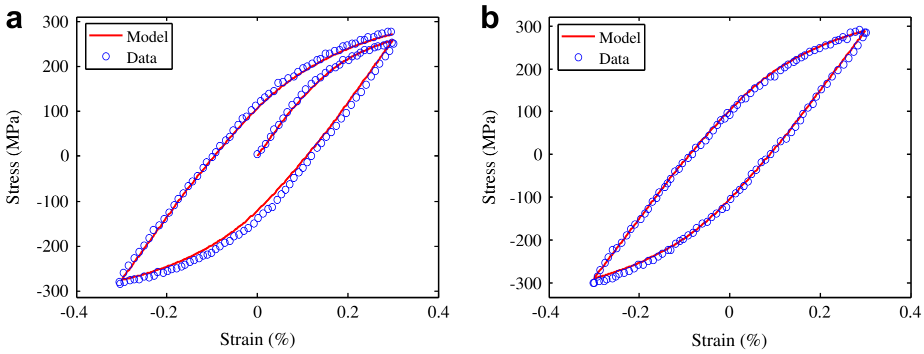

Fig. 13. Comparison of model predictions of cyclic $\sigma - \varepsilon$ behaviour to isothermal experimental data at 600 °C. (a) Monotonic tensile curve and 1st loop and (b) saturated loop.

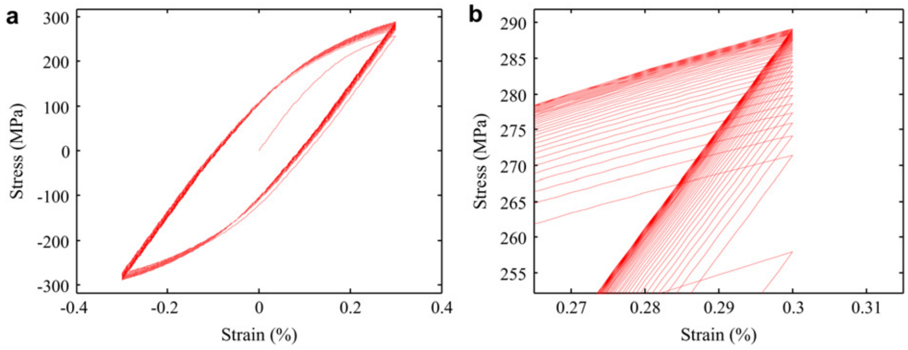

Fig. 15. Full $\sigma - \varepsilon$ model predictions for 50 loops under isothermal conditions at 600 °C. (a) Full loops and (b) zoomed for maximum strain hardening behaviour.

Table 3
Material constants for 316 stainless steel at multiple temperatures.

T (°C)	k (MPa)	E (GPa)	b	Q (MPa)	a_1(MPa)	C_1	a_2(MPa)	C_2	Z (MPa $s^{1/n}$)	n
300	39	154.84	39.46	32.76	119.1	5964.1	108.4	1001.6	179	10
500	32.5	145.54	33.35	30.41	94.6	6472.6	113.3	979.91	175	10
550	31	141.26	31	27.8	86.3	6939	114.8	957.69	173	10
600	30	139.12	28.6	27.43	80.06	7111.9	116	928.7	170	10

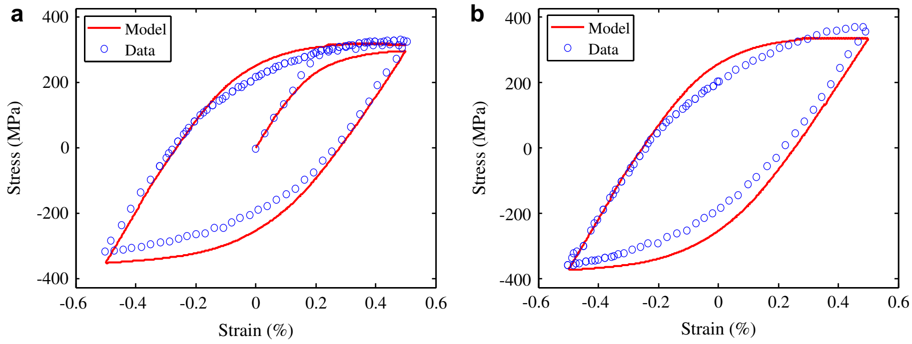

Fig. 16. Comparison of model predictions of cyclic $\sigma - \varepsilon$ behaviour with in-phase TMF experimental data at high strain range. (a) Monotonic tensile curve and 1st loop and (b) saturated loop.

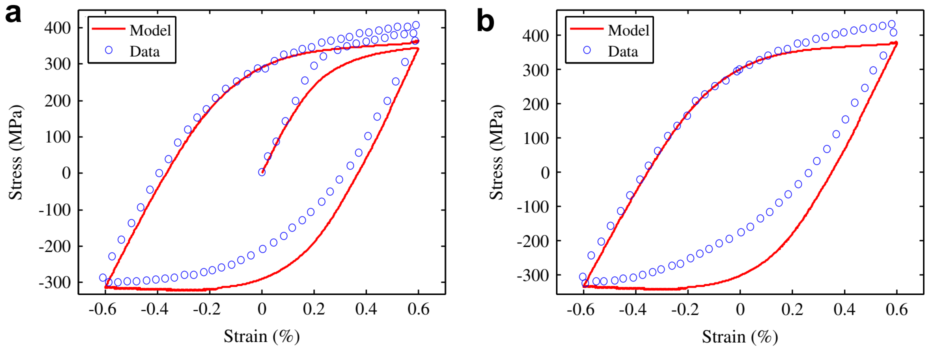

Fig. 17. Comparison of model predictions of cyclic $\sigma - \varepsilon$ behaviour with out-of-phase TMF experimental data at high strain range. (a) Monotonic tensile curve and 1st loop and (b) saturated loop.

model for a temperature of 600 °C, illustrating the predicted cyclic hardening phenomenon (Fig. 12).

5.2. *Comparison of model predictions to anisothermal experimental results*

Table 3 shows that the material constants used in the Chaboche unified viscoplasticity model are generally temperature dependent. Therefore, one way of implementing the anisothermal condition within the model is to identify expressions for the constants as functions of temperature and inputting these expressions to the model rather than single values. This allows each of the constants to be calculated at the beginning of each time increment depending on the value of temperature at the beginning of that time increment. These values are then used in the calculation of the subsequent values of plastic strain, stress, etc., hence creating a temperature-dependent (TMF) material model.

Figs. 16 and 17 show the experimental/model comparisons for the two TMF test conditions.

6. Conclusion

A unified material model, which includes both (non-linear) isotropic and kinematic hardening behaviour as well as viscoplasticity phenomena, such as rate-dependency, has been successfully implemented in Matlab. A programme of isothermal and anisothermal thermo-mechanical tests has been conducted using induction coil heating, with the temperature uniformity controlled to within ±10 °C up to temperatures of 600 °C. The isothermal tests have been employed to identify the material constants for the material model at different temperatures between 300 °C and 600 °C. The experimental data has also been employed to validate the Matlab implementation of the unified viscoplasticity model, showing excellent model to test correlation for the isothermal tests considered. Interpolation of the temperature-dependency of the material constants, for application to the anisothermal simulations, has also shown reasonably good correlation, although the model appears to slightly under-predict the peak tensile stresses during forward plastic deformation and over-predict the intermediate to high compressive stresses during reverse plastic deformation. It is also worth noting that the material constants were obtained only from the ±0.3% strain range (isothermal) data, due to the use of the stepped strain-range technique to minimise specimen usage, whereas the TMF experimental data was obtained at strain ranges of ±0.5% and ±0.6%, the model predictions therefore represent an extrapolation in terms of the strain range used. Further testing to characterise TMF behaviour of the material at the strain range at which the material constants were obtained is expected to improve the anisothermal predictions.

A parallel project is concerned with the development of optimisation techniques for automating and refining the process of material constant identification.

Acknowledgements

The author would like to thank the EPSRC for the funding of this project obtained from the Doctoral Training Programme, and also Steve Williams, Nina Banerjee and Gemma Drew of Rolls-Royce plc for their greatly valued technical support and commitment to the project. Thanks are also given to Tom Buss and Brian Webster for their technical support within the experimentation.

References

[1] Pahlavanyali S, Drew G, Rayment A, Rae CMF. Thermo-mechanical fatigue of a polycrystalline superalloy: the effect of phase angle on TMF life and failure. International Journal of Fatigue 2007;30:330–8.
[2] Evans WJ, Screech JE, Williams SJ. Thermo-mechanical fatigue and fracture if INCO718. International Journal of Fatigue 2007;30:257–67.
[3] Harrison GF, Tranter PH, Williams SJ. Modelling of thermomechanical fatigue in aeroengine turbine blades. In: AGARD conference on thermal mechanical fatigue of aircraft engine materials 161 to 16-12, CP569; 1995.
[4] Dai Y, Marchand NJ, Hongoh M. Fatigue crack growth measurements in TMF testing of titanium alloys using an ACPD technique. Special Applications and Advanced Techniques for Crack Size Determination; 1995:17–32.
[5] Bauschinger J. Ueber die Veranderungen der Elastizitatsgrenze und der festigkeit des Eisens und Stahls durch Strecken, Quetschen, Erwarmen Abkuhlen und durch oftmals wiederholte Belastung, vol. XIII. Munchen: Mitt. Mech-Tech Lab; 1886.
[6] Chaboche JL, Rousselier G. On the plastic and viscoplastic constitutive equations – part 1: rules developed with internal variable concept. Journal of Pressure Vessel Technology 1983;105:153–8.
[7] Chaboche JL, Rousselier G. On the plastic and viscoplastic constitutive equations – part 2: application of internal variable concepts to the 316 stainless steel. Journal of Pressure Vessel Technology 1983;105:159–64.
[8] Lemaitre J, Chaboche JL. Mechanics of solid materials. Cambridge University Press; 1994.
[9] Tong J, Vermeulen B. The description of cyclic plasticity and viscoplasticity of waspaloy using unified constitutive equations. International Journal of Fatigue 2003;25(no. 5):413–20.
[10] Tong J, Zhan ZL, Vermeulen B. Modelling of cyclic plasticity and viscoplasticity of a nickel-based alloy using Chaboche constitutive equations. International Journal of Fatigue 2004;26(8):829–37.
[11] Zhan Z. A study of creep-fatigue interaction in a new nickel-based superalloy. Ph.D thesis, University of Portsmouth; 2004.
[12] Zhan ZL, Tong J. A study of cyclic plasticity and viscoplasticity in a new nickel-based superalloy using unified constitutive equations. Part I: evaluation and determination of material parameters. Mechanics of Materials 2007;39(1):64–72.
[13] Zhan ZL, Tong J. A study of cyclic plasticity and viscoplasticity in a new nickel-based superalloy using unified constitutive equations. Part II: simulation of cyclic stress relaxation. Mechanics of Materials 2007;39(1):73–80.
[14] Zhan Z, Fernando US, Tong J. Constitutive modelling of viscoplasticity in a nickel-based superalloy at high temperature. International Journal of Fatigue 2008;30(7):1314–23.
[15] Santacreu P, Simon C, Coleman A. Thermomechanical fatigue behaviour of stainless steel grades for automotive exhaust manifold applications. Thermomechanical Fatigue Behaviour of Materials 2002;4:227–39.
[16] Rau K, Beck T, Lohe D. Two specimen complex thermal-mechanical fatigue tests on the Austenitic stainless steel AISI 316L. Thermomechanical Fatigue Behaviour of Materials 2002;4:297–311.
[17] Ryu W-S, Kim WG, Lee KY, Yoon KB. Evaluation of creep crack growth behaviour in type 316LN stainless steel. Manuscript for SMiRT 17-NED Special Issue, Korea.
[18] Hyde TH. Creep crack growth in 316 stainless steel at 600 °C. High Temperature Technology 1988;6(2):51–61.
[19] Hyde TH. Anomalous creep behaviour of 316 stainless steel at 550°C. High Temperature Technology 1986;4(1):25–9.
[20] Hyde TH. Creep of 316 stainless steel at 550 and 600 °C and the effects of short duration overloads on creep at 550 °C. Materials at High Temperatures 1997;14(1):27–35.